

Article

Not peer-reviewed version

Inertial Energy Storage Integration with Wind Power Generation by Transgenerator-Flywheel Technology

[Yi Deng](#) * and [Mehrdad Ehsani](#)

Posted Date: 10 June 2024

doi: 10.20944/preprints202406.0536.v1

Keywords: Transgenerator; three-member; dual-mechanical-port (DMP); flywheel distributed energy storage (FDES); wind power generation



Preprints.org is a free multidiscipline platform providing preprint service that is dedicated to making early versions of research outputs permanently available and citable. Preprints posted at Preprints.org appear in Web of Science, Crossref, Google Scholar, Scilit, Europe PMC.

Copyright: This is an open access article distributed under the Creative Commons Attribution License which permits unrestricted use, distribution, and reproduction in any medium, provided the original work is properly cited.

Article

Inertial Energy Storage Integration with Wind Power Generation by Transgenerator-flywheel Technology

Yi Deng ^{1,*} and Mehrdad Ehsani ¹

¹ Department of Electrical and Computer Engineering, Texas A&M University, College Station 77843, USA; yideng0529@tamu.edu; ehsani@tamu.edu.

* Correspondence: yideng0529@tamu.edu

Abstract: A new type of generator, transgenerator, is introduced that integrates the wind turbine and flywheel into one system, aiming to make the flywheel distributed energy storage (FDES) more modular and scalable than the conventional FDES. The transgenerator is a three-member dual-mechanical-port (DMP) machine with two rotating members (inner and outer rotors) and one stationary member (stator). The transgenerator-flywheel system is introduced with its configuration, transgenerator overview, flywheel operation principle and power management strategies, and control system. Simulations are performed in MATLAB/ Simulink to verify the system viability, including control system verification and the flywheel storage performance evaluation. Results show that the inner and outer rotors can be controlled independently with accurate and fast control response, and the grid-side control works properly. The flywheel performs well with considerable charging power and storage capacity.

Keywords: Transgenerator; three-member; dual-mechanical-port (DMP); flywheel distributed energy storage (FDES); wind power generation

1. Introduction

Distributed energy storage (DES) means using energy storage systems distributed throughout the power grids, typically located near the consumer ends [1]. The DES helps balance supply and demand (especially from renewable energy) more timely than centralized energy storage, thus improving the overall grid reliability and resilience. Distributed energy storage is promising in microgrids. Two primary sources of small-scale distributed energy storage are stand-alone batteries and electric vehicles [2].

Flywheel energy storage (FES) is an energy storage type with the advantages of having high power density, high round-trip efficiency (around 90%) [3], long-lasting (typically 20 years or 20,000 cycles or more) [4], cost-effective in the long term, environmentally friendly, and easy to maintain. It is a solution to mitigate the intermittent supply of wind power, and it has been proven efficient in wind energy storage and power smoothing [5–9]. However, FES is viable [10] but not a well-suited candidate for distributed energy storage (DES) due to two main limitations.

One limitation is the energy storage capacity. The capacity of a single flywheel is limited by its physical characteristics and typically ranges from 3 kWh to 133 kWh [11]. Thus, the total flywheel storage is limited if the number of flywheels is insignificant. If the capacity limit issue of the flywheel storage could be addressed, the flywheel can even serve as a battery, providing backup power for a period.

The second limitation concerns the flywheel's connection to the wind turbine. When FES is integrated with wind power generation, there are two typical connection schemes [12]: grid connection and DC link connection, as shown in Figure 1. No matter which connection, a drive motor is needed to drive the flywheel, and the electric converter (converters) is used for the motor. On the one hand, installing the motor and the converter (converters) occupy much space, so flywheels are typically placed on the ground rather than inside the nacelle. On the other hand, when power is

transferred between the flywheel and the grid, it passes through the motor and converters, and each component causes losses during the power exchange process, thus reducing power efficiency. Therefore, equipping one flywheel unit for one wind turbine is not expedient, and FES is thus less modular and distributed than battery energy storage.

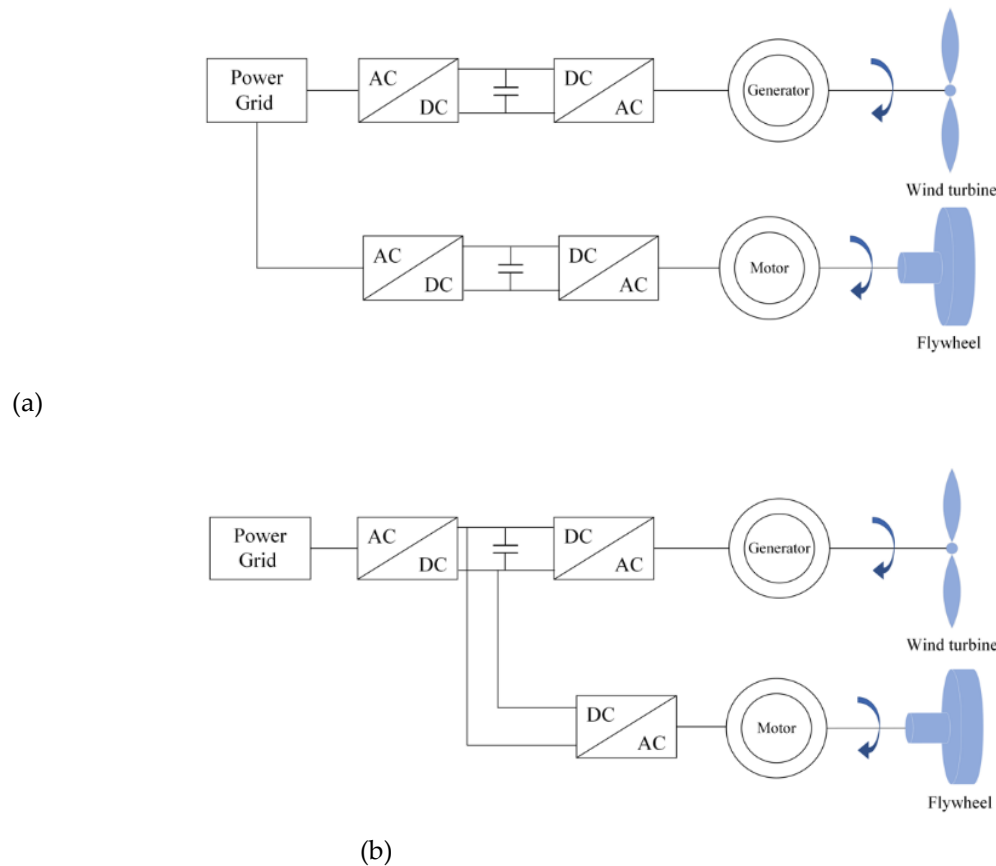
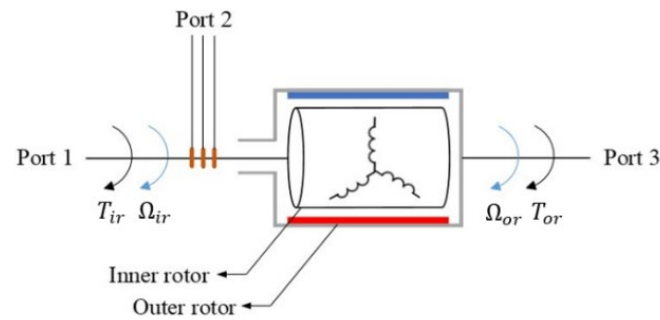
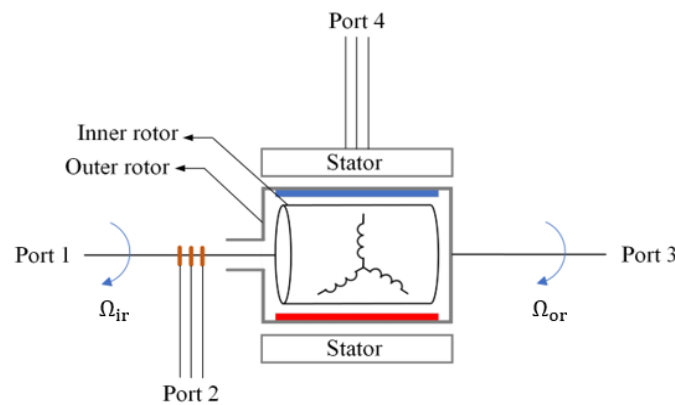


Figure 1. Electric schemes of flywheel connections to wind turbine. (a) grid connection; (b) DC link connection.

One solution is to use a dual-mechanical-port (DMP) generator. Unlike conventional electric machines, which feature one stator and one rotor, the DMP machines have two rotors and do not necessarily have a stator. In 1994, M. Ehsani and S. Sodhi at Texas A&M University introduced a DMP machine consisting of only two rotors, named the “transmotor” [13]. It is also called a two-member transmotor. The diagram of a transmotor is shown in Figure 2 (a). Transmotor signifies the active electromagnetic coupling of the two rotors, enabling the mechanical power transfer directly between the two mechanical ports (Port 1 and Port 3), inner and outer rotor shafts, and the amount of the transferred mechanical power is decided by the electrical port (Port 2), inner rotor windings [13]. This structural innovation aims to enhance energy transfer efficiency. M. Ehsani also proposed a three-member transmotor variation, as shown in Figure 2 (b). The three-member topology has a stator in addition to the two rotors, which provides more control degrees of freedom than the two-member topology, but its control becomes more complicated. Later, L. Xu at Ohio State University furthered the research on DMP machines and mainly focused on the three-member topology [14,15]. The DMP machines have garnered more attention in recent years [16–18].



(a)



(b)

Figure 2. Transmotor diagrams; (a) two-member topology ; (b) three-member topology.

Transmotors have possible applications in electric vehicles (EVs) and hybrid electric vehicles (HEVs) to improve the overall performance of the vehicles [19–24]. Papers [21–24] by M. Ehsani, NF. Ershad, and RT. Mehrjardi explored different applications of transmotors in EVs or HEVs. Although the applications vary, the fundamental idea in these papers is to combine a two-member transmotor with a flywheel as a kinetic energy recovery system (KERS) to increase the compactness and efficiency of the powertrains. Additionally, the flywheel plays a role in alleviating the burden on the vehicle battery by efficiently storing and recovering kinetic energy during deceleration and braking, making the overall vehicle more energy-efficient and sustainable. The DMP machines are rarely considered for wind power generation. In papers [25,26], a three-member DMP generator was used as a variable gearbox with a battery energy storage unit, and a second generator was required to connect to the power grid.

This paper proposed a “Three-member transgenerator-flywheel” system. Its configuration is shown in Figure 3, in which the wound inner rotor is driven by the wind turbine, the PM outer rotor is connected to the flywheel, and the wound stator provides more control degrees of freedom and serves the critical function of achieving independent control of the two rotors for different purposes. This configuration offers several advantages:

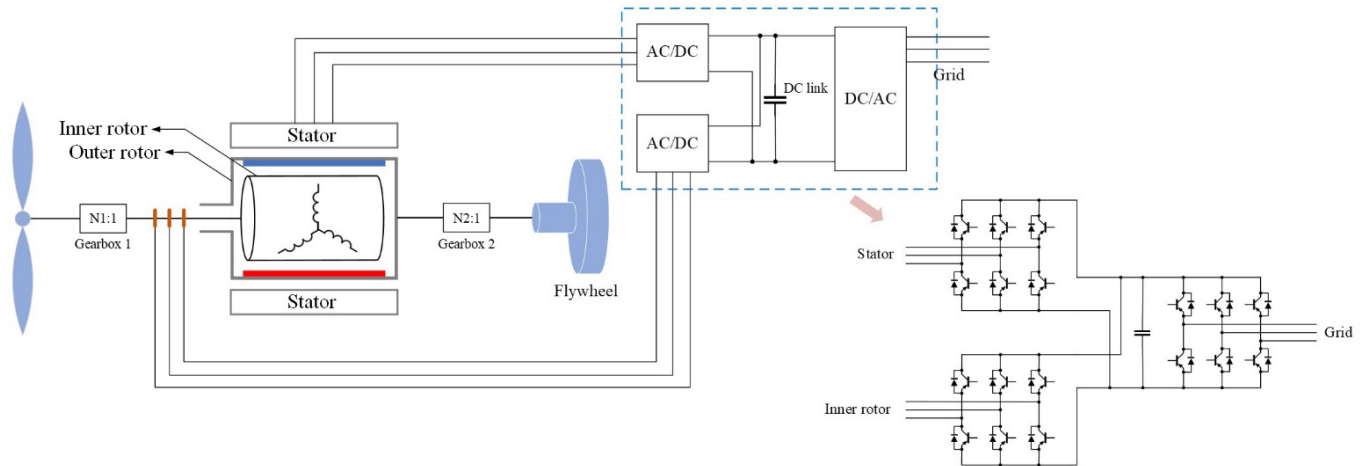


Figure 3. Configuration of the three-member transgenerator-flywheel system.

(1) Compactness: The proposed configuration integrates the wind turbine and flywheel in one system, eliminating the drive motor and converters, making it possible to fit into a turbine nacelle.

(2) Efficiency: The connection between the wind turbine and the flywheel using the proposed configuration creates a shorter path with fewer electrical components for power transfer, which reduces the total power losses and thus increases the overall power efficiency.

(3) Scalability: This configuration ensures one transgenerator is equipped with one flywheel in the wind turbine. The one-to-one feature enables a wind farm to achieve substantial energy storage when the wind turbine number is significant.

(4) Distribution: The one-to-one feature ensures flywheels are as distributed as the wind turbine units. This feature becomes more evident in a wind-based distributed generation (DG) system.

2. Three-Member Transgenerator

2.1. Mathematical Model

2.1.1. Flux Linkage and Voltage Equations

Define the d-axis as aligned with the space vector of the PM rotor flux, λ_{or} . The d-q reference frame is shown in Figure 4. Then, the flux linkage equations are expressed as:

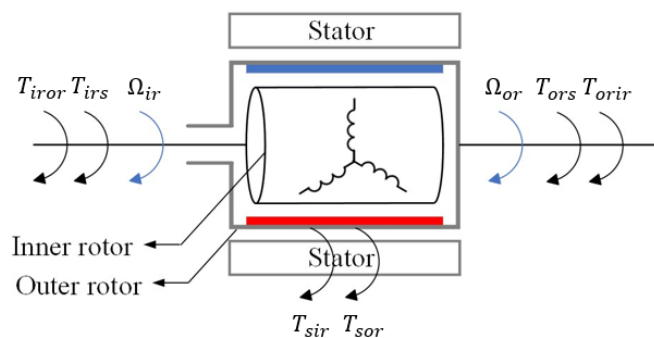
$$\begin{cases} \lambda_{ds} = L_{ds} i_{ds} + L_m i_{dir} + \lambda_{or} \\ \lambda_{qs} = L_{qs} i_{qs} + L_m i_{qir} \\ \lambda_{dir} = L_{dir} i_{dir} + L_m i_{ds} + \lambda_{or} \\ \lambda_{qir} = L_{qir} i_{qir} + L_m i_{qs} \end{cases} \quad (1)$$

Where L_m is the mutual inductance between the stator and inner rotor windings, $L_{\sigma s}$ and $L_{\sigma ir}$ are leakage inductances of the stator and inner rotor. Self-inductance: $L_{ds} = L_{\sigma s} + L_m$, $L_{qs} = L_{\sigma s} + L_m$, $L_{dir} = L_{\sigma ir} + L_m$, $L_{qir} = L_{\sigma ir} + L_m$, thus, $L_{ds} = L_{qs}$ and $L_{dir} = L_{qir}$.

Define the angular frequencies of the inner and outer rotors as ω_{ir} and ω_{or} . Then, the stator angular frequency is ω_{or} since the stator is fixed (no rotation), and the inner rotor slip angular frequency is $(\omega_{or} - \omega_{ir})$. The voltage equations for the stator and inner rotor are as follows:

Where v , i , R , λ , and ω are voltage, current, resistance, flux linkage, and angular velocity, respectively; subscripts d and q mean d , q components, respectively; subscripts ir , or , and s means inner rotor, outer rotor, and stator, respectively.

The torque analysis diagram of the transgenerator is shown in Figure 5. The electromagnetic torque on the outer rotor, T_{eor} , is the sum of two parts: one is from the stator, and the other is from the inner rotor due to the interaction between the magnetic fields produced by the current in the windings. The same analysis method applies to the electromagnetic torques on the inner rotor and stator, T_{eir} and T_{es} , as illustrated in (3)-(5). Note that for the interactive torques, the subscript in the front is the torque-receiving object, and the subscript in the back is the torque-exerting object. E.g., T_{orir} means the torque on the outer rotor exerted by the inner rotor.


$$T_{es} = T_{sor} + T_{sir} \quad (3)$$

$$T_{es} = T_{sor} + T_{sir} \quad (3)$$

$$T_{eir} = T_{irs} + T_{iror} \quad (4)$$

$$T_{eor} = T_{orir} + T_{ors} \quad (5)$$

With (3)-(5), the Figure 4 can be simplified to Figure 6.

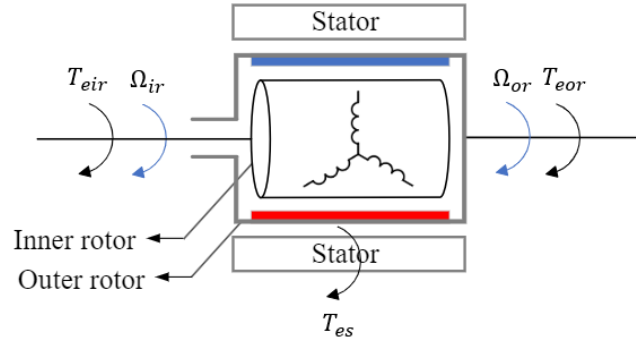


Figure 6. Simplified torque analysis diagram.

Define the angular velocities of the inner and outer rotors as Ω_{ir} and Ω_{or} . With Figure 5, the mechanical power of the inner and outer rotors, P_{eir} and P_{eor} , due to the electromagnetic torques, T_{eir} and T_{eor} , can be calculated as:

$$P_{eir} = T_{eir} \Omega_{ir} \quad (6)$$

$$P_{eor} = T_{eor} \Omega_{or} \quad (7)$$

The total electrical power in the three-phase windings of the stator and inner rotor can be calculated as the dot product of the transpose voltage matrix and the current matrix [27].

$$P_{elec} = \mathbf{v}_{abcs}^t \mathbf{i}_{abcs} + \mathbf{v}_{abcir}^t \mathbf{i}_{abcir} \quad (8)$$

Performing Park transformation to (8) yields the electrical power expression under the d-q frame:

$$P_{elec} = \frac{3}{2} (\mathbf{v}_{dqns}^t \mathbf{i}_{dqns} + \mathbf{v}_{dqnr}^t \mathbf{i}_{dqnr}) \quad (9)$$

Expanding (9) by substituting (2) into it, the expressions for P_{eir} and P_{eor} can be obtained in terms of the flux linkages and currents:

$$P_{eir} = \frac{3}{2} \omega_{ir} (\lambda_{qir} i_{dir} - \lambda_{dir} i_{qir}) \quad (10)$$

$$P_{eor} = \frac{3}{2} \omega_{or} (\lambda_{ds} i_{qs} - \lambda_{qs} i_{ds}) + \frac{3}{2} \omega_{or} (\lambda_{dir} i_{qir} - \lambda_{qir} i_{dir}) \quad (11)$$

When the number of rotor pole pairs is p , the rotors' angular frequencies, ω , and angular velocities, Ω , have the following relations:

$$\omega_{ir} = p \Omega_{ir} \quad (12)$$

$$\omega_{or} = p \Omega_{or} \quad (13)$$

The electromagnetic torques on the inner and outer rotors can be derived in (14) and (15) by substituting (6) and (12) into (10), and (7) and (13) into (11), respectively:

$$T_{eir} = \frac{3}{2} p (\lambda_{qir} i_{dir} - \lambda_{dir} i_{qir}) \quad (14)$$

$$T_{eor} = - \left[\frac{3}{2} p (\lambda_{qs} i_{ds} - \lambda_{ds} i_{qs}) + \frac{3}{2} p (\lambda_{qir} i_{dir} - \lambda_{dir} i_{qir}) \right] \quad (15)$$

According to Newton's third law of motion, for two objects that exist in mutual interaction, the torque exerted on each object by the other is equal in magnitude and opposite in direction. Applying

this law to the transgenerator yields $T_{sor} = -T_{ors}$, $T_{irs} = -T_{sir}$, and $T_{orir} = -T_{iror}$. Using these relations, add (3) and (4):

$$T_{es} + T_{eir} = T_{sor} + T_{iror} = -(T_{ors} + T_{orir}) \quad (16)$$

Observing (16) and (5) yields:

$$T_{eor} = -(T_{es} + T_{eir}) \quad (17)$$

By observing (14), (15), and (17), the stator torque expression can be obtained as :

$$T_{es} = \frac{3}{2} p (\lambda_{qs} i_{ds} - \lambda_{ds} i_{qs}) \quad (18)$$

By substituting (1) into (14) and (18), the torque expressions of the inner rotor and stator can be rewritten as:

$$T_{eir} = \frac{3}{2} p \left[(L_{qir} - L_{dir}) i_{dir} i_{qir} + L_m i_{qs} i_{dir} - L_m i_{ds} i_{qir} - \lambda_{or} i_{qir} \right] \quad (19)$$

$$T_{es} = \frac{3}{2} p \left[(L_{qs} - L_{ds}) i_{ds} i_{qs} + L_m i_{ds} i_{qir} - L_m i_{qs} i_{dir} - \lambda_{or} i_{qs} \right] \quad (20)$$

With $L_{qs} = L_{ds}$ and $L_{qir} = L_{dir}$, (19) and (20) are simplified to (21) and (22), respectively:

$$T_{eir} = \frac{3}{2} p (L_m i_{qs} i_{dir} - L_m i_{ds} i_{qir} - \lambda_{or} i_{qir}) \quad (21)$$

$$T_{es} = \frac{3}{2} p (L_m i_{ds} i_{qir} - L_m i_{qs} i_{dir} - \lambda_{or} i_{qs}) \quad (22)$$

Substituting (21) and (22) into (17) yields:

$$T_{eor} = \frac{3}{2} p \lambda_{or} (i_{qs} + i_{qir}) \quad (23)$$

From (23), the electromagnetic torque on the outer rotor is only related to the q components of the currents in the stator and inner rotor windings since p and λ_{or} are constants.

2.2. Power Flow

The proposed three-member machine is a four-port machine with two mechanical ports (the inner and outer rotors) and two electrical ports (two windings in the stator and inner rotor). The power flow diagram of the three-member machine is illustrated in Figure 7, where P_{eir} and P_{eor} are mechanical power (due to the electromagnetic torques) delivered by the inner rotor and outer rotor, and P_{irw} and P_{sw} are electrical power (due to the electromagnetic induction) received by the windings of the inner rotor and stator.

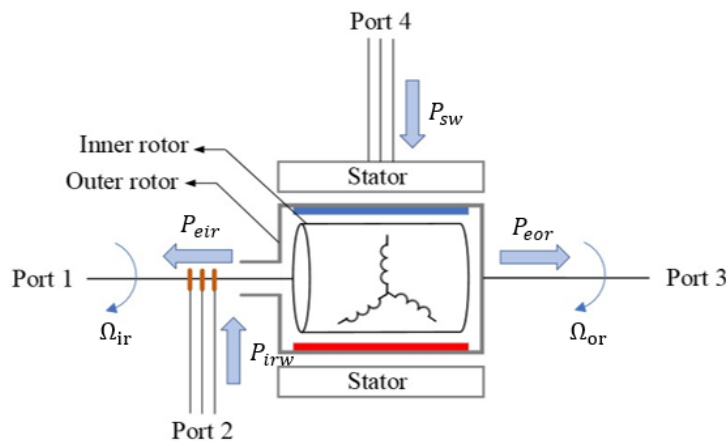


Figure 7. Power flow diagram of the three-member machine.

Let P_{mec} be the total mechanical power delivered by the two rotors, which equals the sum of P_{eor} and P_{eir} , as expressed in (24):

$$P_{mec} = P_{eor} + P_{eir} = T_{eor} \Omega_{or} + T_{eir} \Omega_{ir} \quad (24)$$

The total electrical power received by the windings, P_{elec} , equals the sum of electrical power in the inner rotor and stator windings, P_{irw} and P_{sw} , as expressed in (25):

$$P_{elec} = P_{irw} + P_{sw} \quad (25)$$

When the losses (such as copper and iron losses) are ignored, the total power injected into the machine at each moment is zero, as expressed in (26):

$$P_{eor} + P_{eir} - (P_{irw} + P_{sw}) = 0 \quad (26)$$

That is:

$$P_{mec} = P_{elec} \quad (27)$$

Since the power flow at each port is bidirectional, there are many permutations of the power flow directions. Based on Figure 7, the power flow of the three-member machine can be concluded as follows when all the losses are ignored:

- (1) The electrical power received by the machine, P_{elec} equals the mechanical power delivered by the machine, P_{mec} , at each moment.
- (2) When $P_{elec} (P_{mec}) > 0$, the machine receives electrical power and delivers mechanical power; the machine operates as a transmotor.
- (3) When $P_{elec} (P_{mec}) < 0$, the machine delivers electrical power and receives mechanical power; the machine operates as a transgenerator.

3. Flywheel

3.1. Mechanical System Overview

The mechanical model of the transgenerator-flywheel system consists of two-mass drivetrain models [28], in which two rotating masses are connected through a shaft, as shown in Figure 8. The internal torque is due to the deformation of the connecting shaft, and any material will undergo some degree of deformation. The speed difference of the

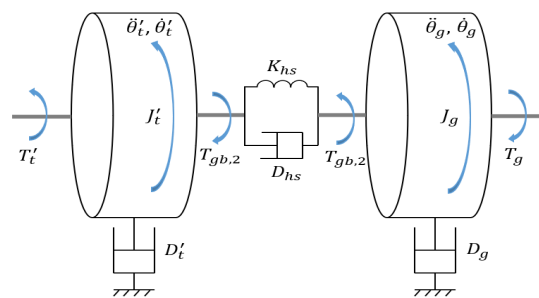


Figure 8. Two-mass drivetrain model.

two masses depends on the flexibility of the shaft. The transgenerator-flywheel system is a dual two-mass drivetrain model, as shown in Figure 9: wind turbine-inner rotor (red) and outer rotor-flywheel (blue); the wind turbine-inner rotor is marked as system 1 and the outer rotor-flywheel is marked as system 2. To simplify the model, the connecting shafts in each system are considered rigid bodies, and all mechanical losses are ignored. Note that each system has a gearbox, and the model analysis is referred to the rotor side. Based on the assumption:

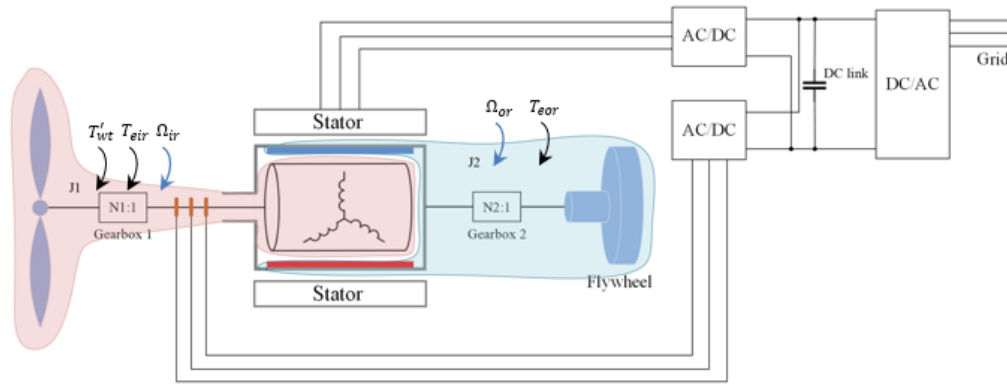


Figure 9. Dual two-mass drivetrain model of the transgenerator-flywheel system.

(1) The total inertia of each system equals the sum inertia of each component referred to the rotor sides; the total inertia of system 1 and system 2 are J_1 and J_2 , respectively.

(2) The rotational speed of system 1 is consistent with the inner rotor's angular velocity, Ω_{ir} ; the speed of system 2 is consistent with the outer rotor's angular velocity, Ω_{or} .

(3) The torques on system 1 include torque on the wind turbine referred to the inner rotor side, T'_{wt} , and the electromagnetic torque on the inner rotor, T'_{eir} ; the torque on system 2 is the electromagnetic torque on the outer rotor, T'_{eor} .

3.2. Flywheel Charging Power and Storage Energy

With the simplified mechanical model in Figure 9, the charging power of the flywheel, P_{fw} , equal to the mechanical power of the outer rotor, P_{eor} , can be calculated as the product of the outer rotor torque and angular velocity (speed):

$$P_{fw} = P_{eor} = T_{eor} \Omega_{or} \quad (28)$$

Based on the torque and speed directions in Figure 9, when the power, P_{fw} , is positive, the flywheel receives power from the transgenerator, the flywheel is charged; when the power is negative, the flywheel delivers power to the transgenerator, the flywheel is discharged.

The energy stored in the flywheel can be calculated with the flywheel inertia (referred to the rotor side) and the outer rotor speed:

$$E_{fw} = \frac{1}{2} J'_{fw} \Omega_{or}^2 \quad (29)$$

where J'_{fw} is the flywheel inertia referred to the rotor side, which has the following relationship with the actual flywheel inertia, J_{fw} , and the gearbox ratio between the outer rotor and flywheel, N_2 .

$$J'_{fw} = J_{fw} N_2^2 \quad (30)$$

The actual flywheel speed, Ω_{fw} , can be calculated with the outer rotor speed and the gearbox ratio, N_2 :

$$\Omega_{fw} = \Omega_{or} N_2 \quad (31)$$

With the actual flywheel speed obtained, the energy stored in the flywheel can also be expressed with the actual flywheel inertia and speed:

$$E_{fw} = \frac{1}{2} J_{fw} \Omega_{fw}^2 \quad (32)$$

If the maximum speed of the flywheel is $\Omega_{fw,max}$, the storage capacity of the flywheel is:

$$E_{fw, capacity} = \frac{1}{2} J_{fw} \Omega_{fw, max}^2 \quad (33)$$

If the flywheel decelerates from a higher speed, Ω_{fw2} , to a lower speed, Ω_{fw1} , the energy released from the flywheel ΔE_{fw} , is:

$$\Delta E_{fw} = \frac{1}{2} J_{fw} (\Omega_{fw2}^2 - \Omega_{fw1}^2) \quad (34)$$

3.3. Flywheel Power Management Strategies

According to (28), flywheel power can be managed by changing the outer rotor torque, outer rotor speed, or both. The analysis is as follows:

- (1) Due to the acceleration, the speed change in the flywheel cannot be furnished immediately, delaying the power response to the demand. Therefore, changing the outer rotor torque is a better strategy.
- (2) To ensure the accuracy of the power control by controlling the outer rotor torque, the speed changes slightly in a short period, which requires the flywheel inertia referred to the outer rotor side to be significant.
- (3) Before the flywheel power management process, the flywheel should be accelerated to a state of charge (SOC) to ensure that the flywheel can release enough energy during emergencies. Besides, there should be a margin with the maximum storage to leave enough space for charging. The preset flywheel SOC in this paper is 80%, and then the flywheel speed will fluctuate (slightly most of the time) at around 80% SOC, as shown in Figure 10.

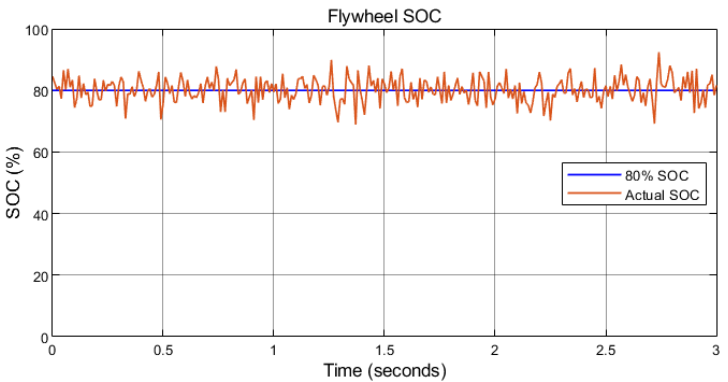


Figure 10. Flywheel SOC illustration.

- (4) The performance of flywheel power response depends on the performance of the outer rotor torque control, which will be introduced later.

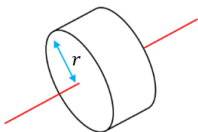
3.4. Flywheel Selection

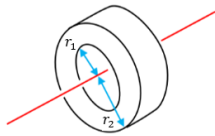
3.4.1. Shape

The flywheel shapes are typically disc or ring, so the flywheel selection in this paper is over these two. As shown in Table 1, the inertia of the ring-shaped flywheel is greater than that of the disc flywheel when they have the same mass and radius ($r = r_2$). To achieve the same mass, when the radius of the disc-shape flywheel equals the outer radius of the ring-shape flywheel ($r = r_2$), and they have the same material density, ρ is the same, the mass and volume has the relation below:

$m = \rho V$ (35)

Table 1. Moment of Inertia of disc flywheel and ring flywheel.

Shape	Description	Moment of Inertia
	Solid cylinder (or disk) of radius r .	$J = \frac{1}{2}mr^2$



Annular cylinder (or ring) of inner radius r_1 and outer radius r_2 .

$$J = \frac{1}{2} m(r_1^2 + r_2^2)$$

That means their volumes should be equal. The volume of the disc flywheel, V_{disc} , and the ring flywheel, V_{ring} , are calculated as follows:

$$V_{disc} = \pi r^2 h_{disc} \quad (36)$$

$$V_{ring} = \pi (r_2^2 - r_1^2) h_{ring} \quad (37)$$

Where h_{disc} and h_{ring} are the thicknesses of the disc and ring flywheels, respectively. Since $r = r_2$, $r^2 > (r_2^2 - r_1^2)$, when $V_{disc} = V_{ring}$, $h_{disc} < h_{ring}$. That means when the volumes are equal, the ring-shaped flywheel is thicker than a disc-shaped flywheel if they have the same radius and density of the material. However, according to the calculation, the effect of the thickness on the nacelle horizontal space is ignorable. Thus, the ring-shaped flywheel is selected.

3.4.2. Material

The flywheel in this paper is decided on steel for the following reasons. First, the high density of steel (7850 kg/m³) helps reduce the flywheel size compared to the lower-density materials. Second, steel has a strong tensile strength (around 70,000 psi and decent yield strength (around 50,000 psi), which allows the flywheel to withstand high-speed rotation. The chart of strength [29] shows the strength of different materials. Further, the steel prices are not expensive compared to many other materials, which is cost-effective. A chart of prices in paper [30] shows the prices of different materials.

4. Control System

The control system consists of rotor-side and grid-side control based on field-oriented control (FOC) [31]. The control details are not illustrated in this paper.

4.1. Rotor-Side Control

The goal of rotor-side control is to control each rotor independently to achieve speed control on the inner rotor side and torque control on the outer rotor side for different purposes.

4.1.1. Inner Rotor Speed Control

The inner rotor control aims to achieve maximum power point tracking (MPPT). The MPPT control applies indirect torque control [24], as shown in Figure 11. The MPPT algorithm is the higher-level control, producing the speed reference for the lower-level control. Thus, speed control is applied to the inner rotor since the wind turbine is connected to it.

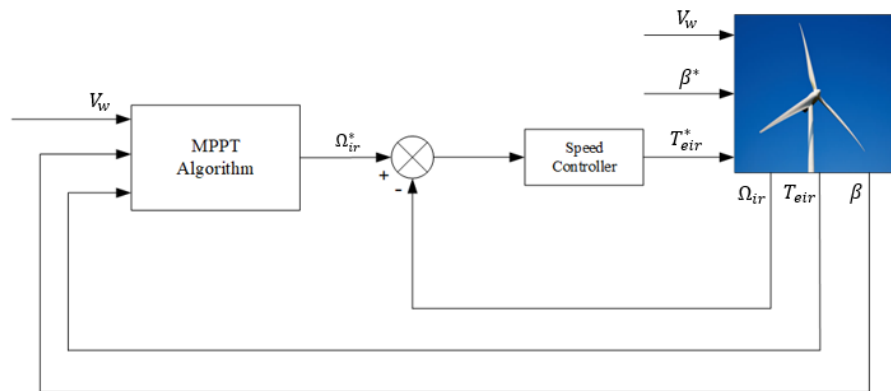


Figure 11. Inner rotor control scheme (MPPT).

4.1.2. Outer Rotor Torque Control

As illustrated in Section 3.3, the outer rotor-side control aims to manage the flywheel charging/discharging power by controlling the outer rotor torque. The outer rotor control scheme is shown in Figure 12, in which the flywheel energy storage (FES) management algorithm (not discussed in this article) is the higher-level control, producing the torque control reference for the lower-level control.

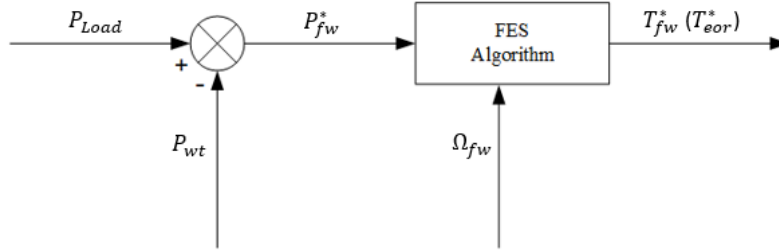


Figure 12. Outer rotor control scheme.

4.1.3. Rotor-Side Control Diagram

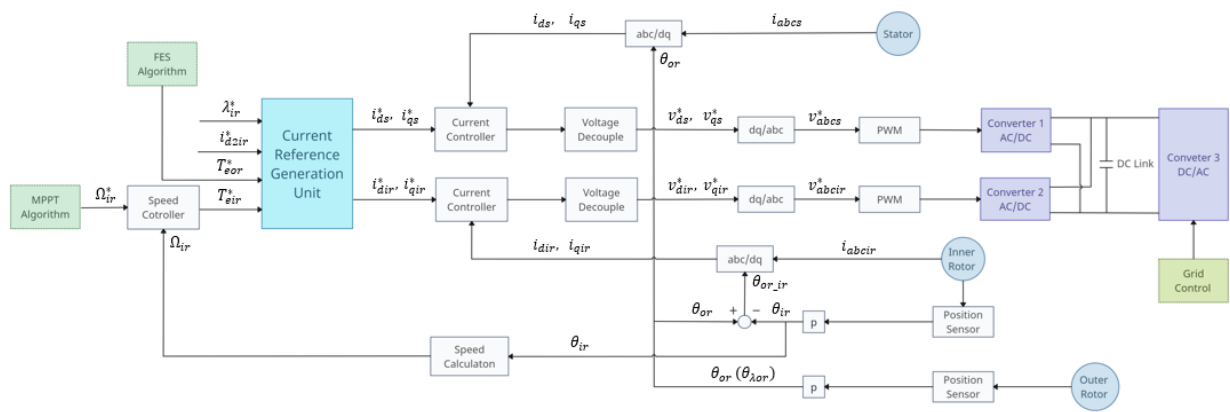


Figure 13. Rotor-side control diagram.

4.2. Grid-Side Control

The purpose of the grid-side control is to maintain the DC link voltage constant and control the reactive power from the grid-side converter to the grid. In the grid-side control, the space vector sum of the grid voltage, \vec{v}_g , is aligned with the d-axis (a different d-q axis from the rotor-side control). The grid-side control diagram is shown in Figure 14.

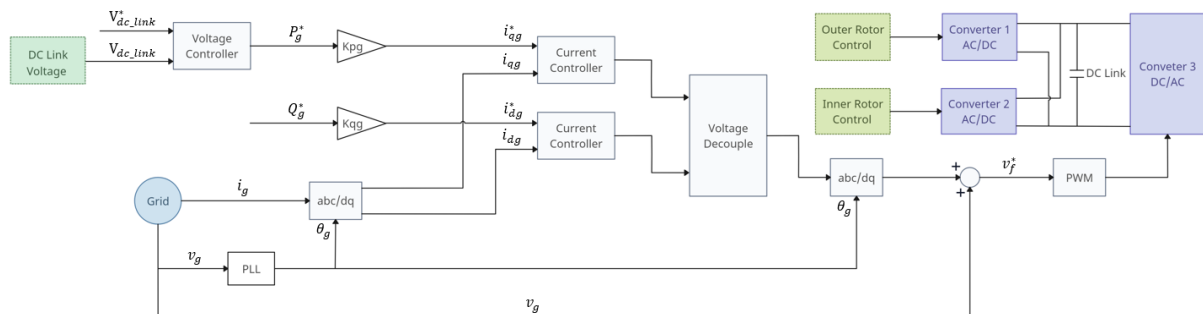


Figure 14. Grid-side control diagram.

5. Simulation and Verification

5.1. Simulink Modeling

System modeling is in MATLAB/Simulink. The modeling includes the wind turbine, transgenerator-flywheel system, and control system.

The wind turbine model generates the torque on the wind turbine, T'_{wt} , from the wind power. Its modeling is based on the aerodynamic model, as shown in Figure 15. The rated power of the wind turbine is 2 MW with a rated wind speed of 10 m/s. The parameters are shown in Table 2. The parameters are determined based on a series of 2 MW wind turbines.

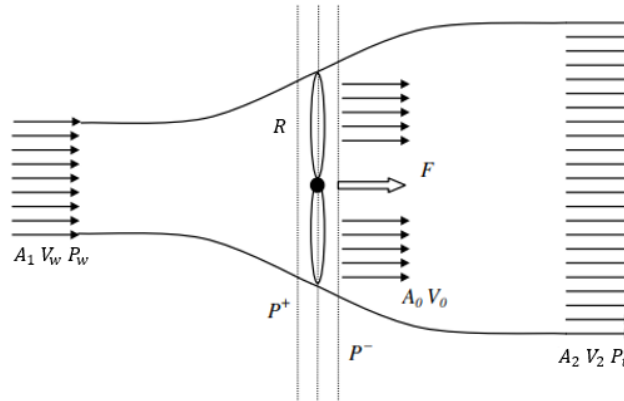


Figure 15. Aerodynamic model of wind turbine.

Table 2. Wind turbine parameters.

Parameter	Value
Rated power	2 MW
Blade radius	50 m
Blade inertia	$6 \times 10^6 \text{ kg}\cdot\text{m}^2$
Rated wind speed	10 m/s
Air density	1.225 kg/m ³

Transgenerator-flywheel modeling: the electrical part modeling of the transgenerator is based on the flux linkage and voltage equations in (1) and (2). The parameters of the electrical system are shown in Table 3. The mechanical part modeling is based on the simplified dual two-mass drivetrain model in Figure 9. The parameters of the mechanical system are shown in Table 4, in which all the components are referred to the rotor side. The flywheel modeling is based on the flywheel selection in Section 3.4. The flywheel parameters are shown in Table 5.

Table 3. Electrical parameters of the transgenerator.

Parameter	Value
Rated stator voltage (line-to-line)	690 V _{rms}
Rated inner rotor voltage (line-to-line)	915 V _{rms}
Pole pairs number p	3
Stator to inner rotor turns ratio	1:1
Mutual inductance L_m	2.6 mH
Inner rotor leakage inductance $L_{\sigma ir}$	0.1 mH
Stator leakage inductance $L_{\sigma s}$	0.1 mH
Inner rotor resistance R_{ir}	$1.5 \times 10^{-3} \Omega$
Stator resistance R_s	$1.2 \times 10^{-3} \Omega$
Outer PM rotor flux λ_{or}	2 Wb

Table 4. Mechanical parameters of the transgenerator.

Parameters	Value
System 1 inertia J_1	3000 kg·m ²
System 2 inertia J_2	32000 kg·m ²
Rated Inner rotor torque	32739 N·m
Rated Outer rotor torque	5300 N·m
Gear ratio N_1	45
Gear ratio N_2	10

Table 5. Flywheel parameters.

Parameters	Type/Value
Shape	Ring
Material	Steel
Density	7850 kg/m ³
Inner radius r_1	0.5 m
Outer radius r_2	0.6 m
Thickness h	0.3624 m
Mass	983.7 kg
Inertia J_{fw}	300 kg·m ²

Control system modeling is based on the control diagrams in Figure 13 and Figure 14 for rotor-side control and grid-side control, respectively.

5.2. Control System Verification

This section aims to evaluate the control accuracy and time response. The simulation duration is 95 seconds: 0-65 s is for the outer rotor torque control verification, 65-95 s is for inner rotor speed control verification, and the grid-side control verification is throughout the simulation.

5.2.1. Set Up

- Outer rotor torque control

To verify the outer rotor torque control, set a series of constant torque references for the outer rotor and observe the actual torque response (outer control loop) and corresponding currents response (inner control loops). Also, ensure the outer rotor speed changes with torque correctly. Note that the outer rotor torque limit range is -5300 N to 5300 N. Meanwhile, the wind speed of 8 m/s for the wind turbine and the MPPT unit is set to generate corresponding constant wind turbine torque and inner rotor speed reference during the outer rotor torque control verification.

(1) 0-10 s, the inner rotor accelerates to a constant speed, and the outer rotor torque is set to zero (turbine start-up). The initial speed of the outer rotor is 30 rad/s.

(2) 10-65 s, the outer rotor torque reference is set every 5 seconds, and the values are: 1000 N·m, 2000 N·m, 3000 N·m, 4000 N·m, 5000 N·m -1000 N·m, -2000 N·m, -3000 N·m, -4000, -5000 N·m, and 0.

- Inner rotor speed control

To verify the inner rotor speed control, set a series of constant wind speeds for the wind turbine and the MPPT unit to generate a series of corresponding wind turbine torques and inner rotor speed references. Observe the actual speed response (outer control loop), corresponding torque response, and current response (inner control loops). From 65-95 s, the wind speed is set every 5 seconds, and the values are: 9 m/s, 10 m/s, 9m/s, 8 m/s, 7 m/s, and 6 m/s.

- Grid-side control

To verify the grid-side control, set the DC link voltage reference to 1300 V and the grid reactive power reference to -200 kVar. Observe the actual voltage and reactive power response (outer control loops), active power response, and current response (inner control loops).

5.2.2. Results

- Outer rotor torque control

The outer rotor torque control results are shown in Figure 16 (a) (the top two figures) and Figure 16 (b) from 0 to 65 s. Note that the blue lines represent the actual values, and the green lines represent the control references. As shown in Figure 16 (a), as the torque reference changes, the actual torque can quickly track the reference (around 1 s) with a slight overshoot. The outer rotor accelerates/decelerates with correct accelerations as the torque changes. Meanwhile, the d-q components of the stator and inner rotor currents track the current references promptly, as shown in Figure 16 (b) (0-65 s). Thus, the outer rotor control is verified.

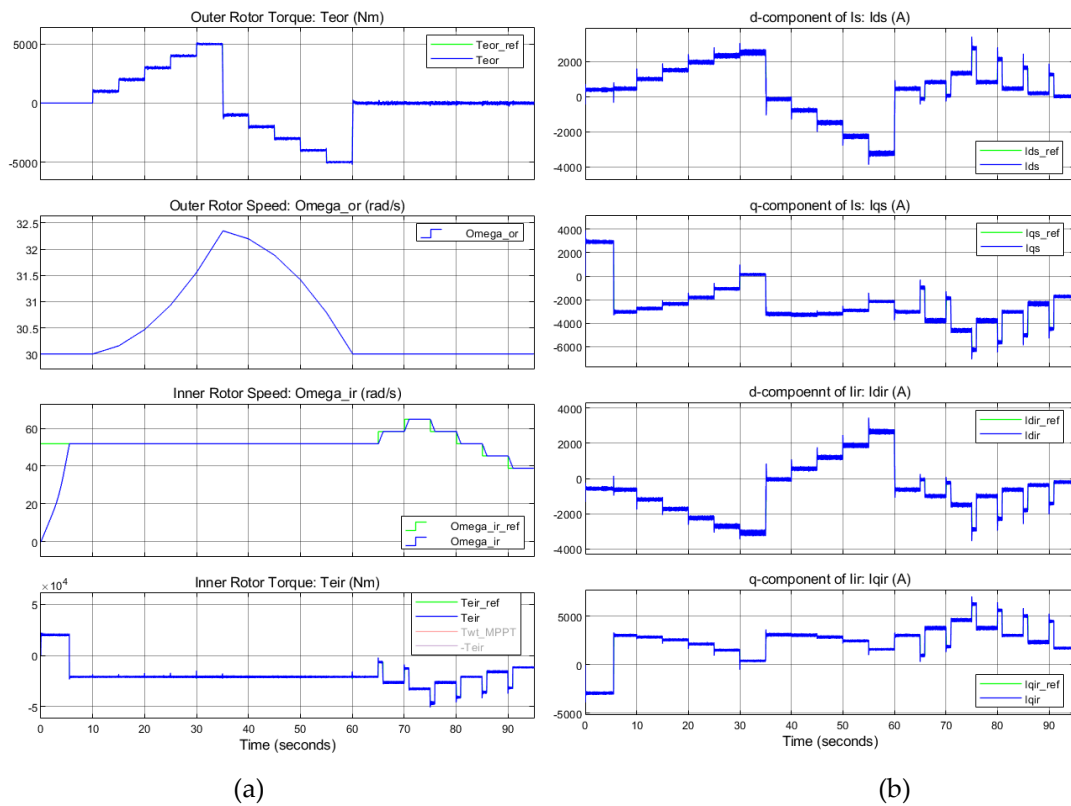


Figure 16. Verification of the rotor-side control. (a) Outer control loops; (b) inner control loops.

- Inner rotor speed control

The inner rotor speed control results are shown in Figure 16 (a) (the bottom two figures) and Figure 16 (b) from 65 to 95 s. Figure 16 (a) shows that the speed can converge to the reference within 1.2 seconds. The actual inner rotor torque tracks the torque reference generated by the speed controller. The inner rotor acceleration is determined by T_{wt_MPPT} and the inner rotor torque. Meanwhile, the d-q components of the stator and inner rotor currents track the current references promptly, as shown in Figure 16 (b) (65-95 s). Thus, the inner rotor control is verified.

- Three-phase currents and voltage on the rotor side

Figure 17 shows the waveforms of the stator and inner rotor's three-phase voltages and currents. The voltages are square waves from the converter sides, and the currents are sine waves. The frequencies in the stator and inner rotor windings match the corresponding slip angular velocities and angular frequencies.

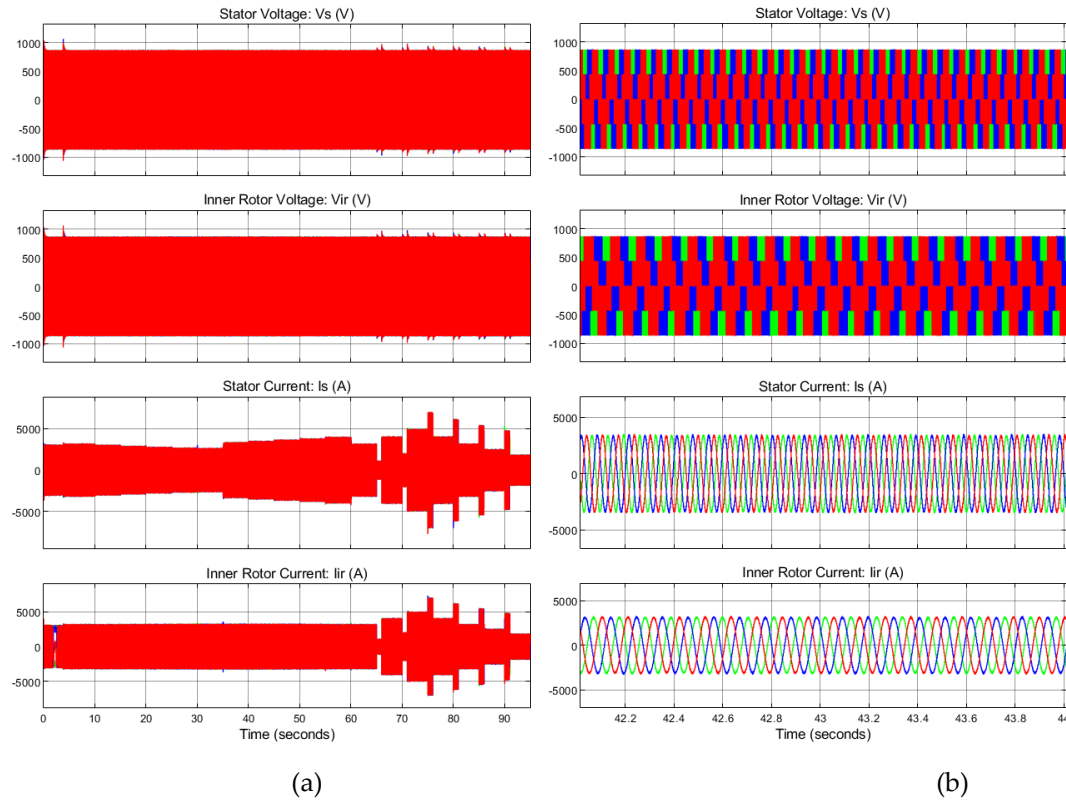


Figure 17. Three-phase voltages and currents of the stator and inner rotor; (b) Zoom-in waveforms at around 43 s.

- Grid-side control

The grid-side control results are shown in Figure 18. From Figure 18 (a), the DC link voltage and the grid reactive power keep track of their references during the simulation. The actual active power on the grid side tracks the active power reference. Meanwhile, the d-q current components track the current reference with a timely response, as shown in Figure 18 (b). The change in the active power is closely related to the reference values change on the generator (rotors) side, mainly the inner rotor (wind turbine). Thus, the grid-side control is verified.

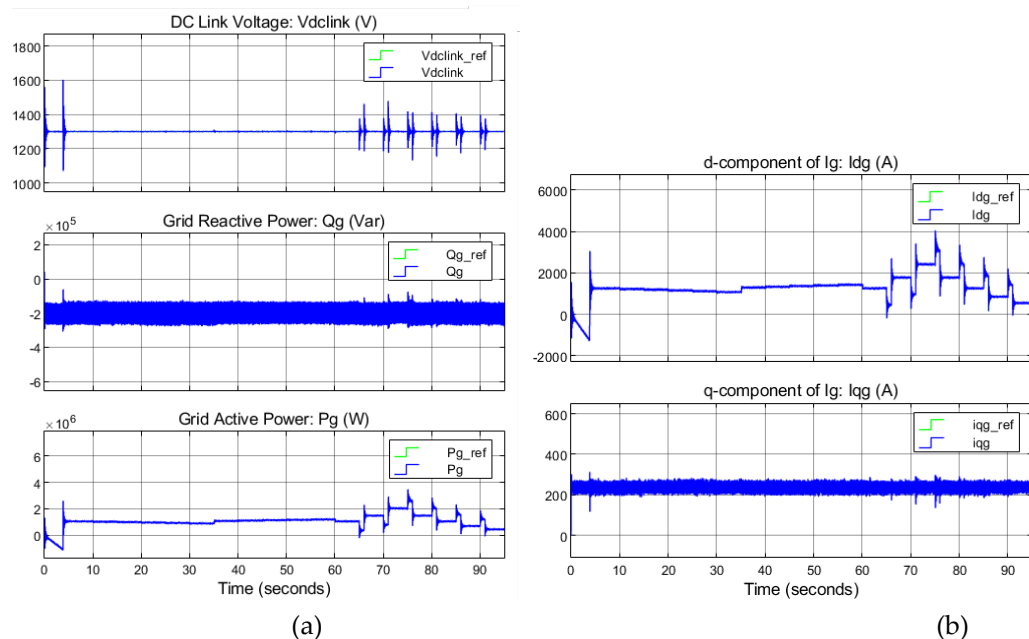


Figure 18. Verification of the grid-side control. (a) Outer control loops; (b) inner control loops.

- Three-phase current and voltage on the grid side

Figure 19 shows the waveforms of the grid-side three-phase voltages and currents. The voltages on the converter side are square waves, while the voltages on the grid side and the currents are sine waves with a frequency of 60 Hz.

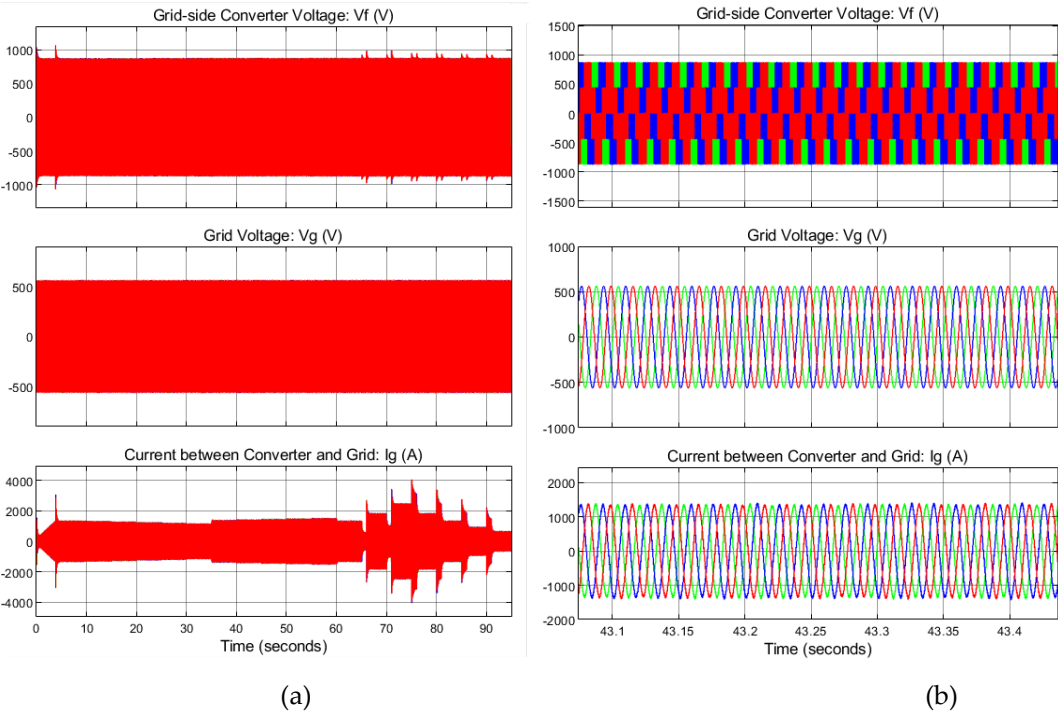


Figure 19. Grid-side three-phase voltages and currents; (b) Zoom-in waveforms at around 43.2 s.

5.3. Flywheel Performance Evaluation

Section 3.3 introduces the flywheel power management strategies, and the flywheel parameters are shown in Table 5. Table 6 shows the flywheel performance parameters.

Table 6. Flywheel performance parameters.

Parameters	Value
Outer rotor speed limit	125 rad/s
Flywheel speed limit	1250 rad/s (11937 rpm)
Storage capacity	65.1 kWh

5.3.1. Set up

The simulation duration is 65 seconds. The initial speed of the outer rotor is set to 100 rad/s (80% SOC). 0-10s is for the wind turbine start-up process under the wind speed of 8 m/s. 10-65 s is for flywheel charging/discharging. To simplify the FES management unit, set a series of outer rotor torque reference values every 5 seconds, and the values are: 1000 N·m, 2000 N·m, 3000 N·m, 4000 N·m, 5000 N·m, -1000 N·m, -2000 N·m, -3000 N·m, -4000, -5000 N·m, and 0, as shown in Figure 20. Observe the power response of the flywheel.

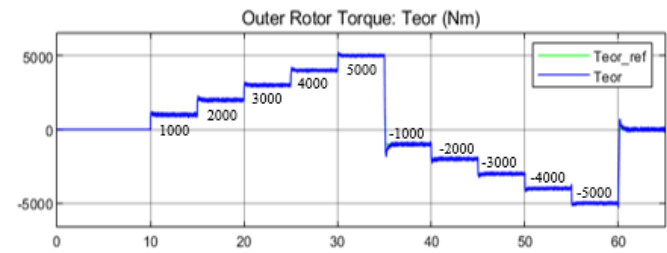


Figure 20. Outer rotor torque command.

5.3.2. Results

Figure 21 shows the outer rotor speed, and the power plots are shown in Figure 22. Note that the power flow directions in the modeling are consistent with those in Figure 7.

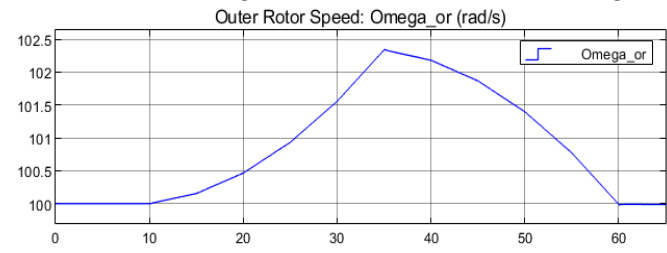


Figure 21. Outer rotor speed.

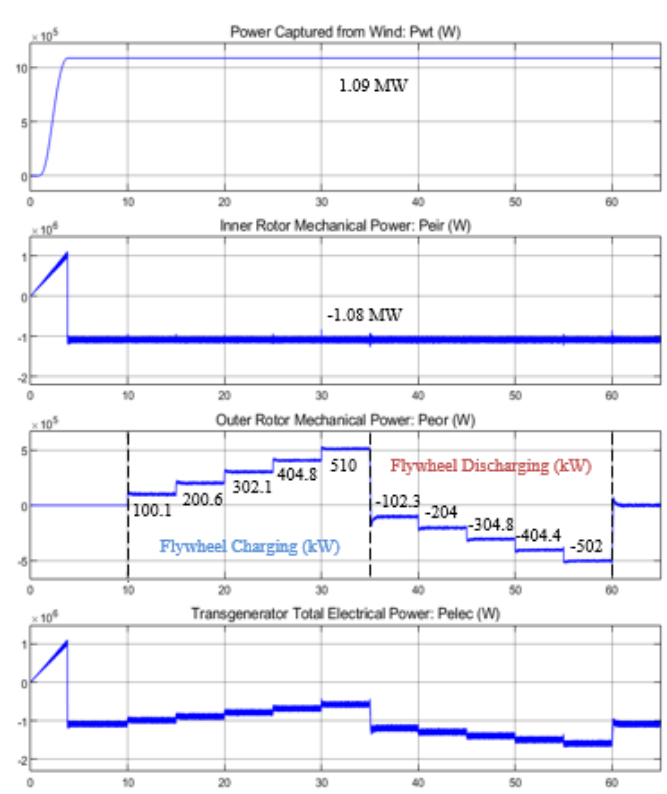


Figure 22. Power polts. 1st: Electrical power generated from the wind turbine; 2nd: Mechanical power delivered by the inner rotor; 3rd: mechanical power delivered by the outer rotor; 4th: total electrical power received by the transgenerator.

(1) 0-10 s, after the inner rotor start-up process, the power generated by the wind turbine is 1.09 MW, as shown in the 1st plot of Figure 22; The power delivered by the inner rotor is -1.08 MW,

meaning the inner rotor receives 1.08 MW of power from the wind turbine, as shown in the 2nd plot in Figure 22.

(2) 10-35 s, the outer rotor accelerates (flywheel) in a series of increasing positive accelerations, and the flywheel is charged, as shown in the 3rd plot in Figure 22.

(3) 35-60 s, the outer rotor (flywheel) decelerates in a series of increasing negative accelerations, and the flywheel is discharged, as shown in the 3rd plot in Figure 22.

(4) 60-65 s, the acceleration of the outer rotor is 0, and the flywheel is neither charged nor discharged, as shown in the 3rd plot in Figure 22.

(5) 10-65 s, the total electrical power received by the transgenerator is negative (power generated by the transgenerator is positive), and it changes with the flywheel charging power in real-time, as shown in the 4th plot in Figure 22.

The 3rd power plot in Figure 22 also indicates that the flywheel responds quickly to the outer rotor torque command (reference) and delivers accurate power. The maximum power at 80% is slightly higher than 510 kW (since the outer torque limit is 5300 N·m, but the maximum power in the simulation is 5000 N·m), about 27% of the wind turbine's rated power). The torque direction decides the power flow direction. Besides, the torque has little effect on the flywheel speed due to its significant inertia (referred to the outer rotor side). Hence, the charging power changes slightly for a specific torque command, as shown in Figure 21, ensuring the accuracy of flywheel power delivery. Overall, the flywheel performs as expected.

6. Conclusion

This paper presented a three-member transgenerator-flywheel system for wind power generation, which is a new flywheel energy storage (FES) concept that the flywheel can be directly integrated with the wind turbine using the dual-mechanical-port (DMP) generator (transgenerator). This configuration makes the FES more modular and distributed than the conventional FES system. The system was introduced by transgenerator, flywheel (from the principle, power characteristics in the transgenerator-flywheel system, energy management strategies, and flywheel selection considerations), and control system. System modeling and simulations were conducted with Simulink. The first part of the simulation verified the accuracy and time response of the control over the two rotors with the outer and inner control loops. The control for both rotors had a quick and accurate response. The second part of the simulation evaluated the flywheel storage performance. The results showed that the flywheel had a maximum charging power of 27% of the wind turbine's rated power at 80% SoC. The flywheel could rapidly and accurately respond to the power demand due to the excellent time response of the outer rotor torque control and its ability to maintain speed.

References

1. Y.-C. Tsao and T.-L. Vu, "Distributed Energy Storage System Planning in relation to Renewable Energy Investment," *Renewable Energy*, vol. 218, p. 119271, Dec. 2023.
2. C. Frischmann, J. P. Gouveia, and A. Horowitz, "Distributed Energy Storage @ projectdrawdown #climatesolutions," *Project Drawdown*, <https://drawdown.org/solutions/distributed-energy-storage>.
3. K. Fitton, "Storing renewable electricity on the grid of the future (updated for 2023)," Medium, <https://medium.com/@kitfitton/storing-renewable-electricity-on-the-grid-of-the-future-updated-for-2023-1816484dc9cd>.
4. D. W. Gao, "Basic Concepts and Control Architecture of Microgrids," in *Energy Storage for Sustainable Microgrid*, Denver, Colorado: University of Denver, 2015, pp. 1–34.
5. G. O. Suvire, M. G. Molina, and P. E. Mercado, "Improving the integration of wind power generation into AC microgrids using flywheel energy storage," *IEEE Transactions on Smart Grid*, vol. 3, no. 4, pp. 1945–1954, Dec. 2012.
6. A. S. Mir and N. Senroy, "Intelligently controlled flywheel storage for enhanced dynamic performance," *IEEE Transactions on Sustainable Energy*, vol. 10, no. 4, pp. 2163–2173, Oct. 2019.
7. S. Gayathri Nair and N. Senroy, "Wind turbine with flywheel for improved power smoothening and LVRT," *2013 IEEE Power & Energy Society General Meeting*, 2013.
8. F. Díaz-González, A. Sumper, O. Gomis-Bellmunt, and F. D. Bianchi, "Energy Management of flywheel-based energy storage device for wind power smoothening," *Applied Energy*, vol. 110, pp. 207–219, Oct. 2013.

9. X. Li and A. Palazzolo, "A review of Flywheel Energy Storage Systems: State of the art and opportunities," *Journal of Energy Storage*, vol. 46, p. 103576, Feb. 2022.
10. M. G. Molina, "Distributed Energy Storage Systems for Applications in Future Smart Grids," *2012 Sixth IEEE/PES Transmission and Distribution: Latin America Conference and Exposition (T&D-LA)*, Sep. 2012.
11. "Flywheel energy storage," Wikipedia, https://en.wikipedia.org/wiki/Flywheel_energy_storage.
12. S. M. Mousavi G, F. Faraji, A. Majazi, and K. Al-Haddad, "A comprehensive review of Flywheel Energy Storage System Technology," *Renewable and Sustainable Energy Reviews*, vol. 67, pp. 477–490, Jan. 2017.
13. S. Sodhi, "Electromagnetic gearing applications in hybrid-electric vehicles," *Ph.D. thesis*, Texas A&M University, 1994.
14. L. Xu, "A new breed of electric machines - basic analysis and applications of dual mechanical port electric machines," *2005 International Conference on Electrical Machines and Systems*, 2005.
15. H. Cai and L. Xu, "Modeling and control for cage rotor dual mechanical port electric machine—part I: Model development," *IEEE Transactions on Energy Conversion*, vol. 30, no. 3, pp. 957–965, 2015.
16. R. He and J. Li, "Optimized design and performance analysis of a magnetic-field modulated brushless dual-mechanical port motor with Halbach Array Permanent magnets," *Advances in Mechanical Engineering*, vol. 12, no. 9, p. 168781402095775, Sep. 2020.
17. H. Chen et al., "Comparative study and design optimization of a dual-mechanical-port electric machine for Hybrid Electric Vehicle Applications," *IEEE Transactions on Vehicular Technology*, vol. 71, no. 8, pp. 8341–8353, Aug. 2022.
18. M. Jiang and S. Niu, "Overview of dual mechanical port machines in transportation electrification," *IEEE Transactions on Transportation Electrification*, pp. 1–1, 2024.
19. Y. Gao and M. Ehsani, "A mild hybrid vehicle drive train with a floating stator motor-configuration, control strategy, design and simulation verification," *SAE Technical Paper Series*, 2002.
20. H. Nasiri, A. Radan, A. Ghayebloo, and K. Ahi, "Dynamic modeling and simulation of transmotor based series-parallel HEV applied to Toyota Prius 2004," *2011 10th International Conference on Environment and Electrical Engineering*, 2011.
21. N. Farrokhzad Ershad, R. T. Mehrjardi, and M. Ehsani, "Electro-mechanical EV powertrain with reduced volt-ampere rating," *IEEE Transactions on Vehicular Technology*, vol. 68, no. 1, pp. 224–233, 2019.
22. N. F. Ershad, R. T. Mehrjardi, and M. Ehsani, "Development of a kinetic energy recovery system using an active electromagnetic slip coupling," *IEEE Transactions on Transportation Electrification*, vol. 5, no. 2, pp. 456–464, 2019.
23. R. Tafazzoli Mehrjardi, N. F. Ershad, and M. Ehsani, "Transmotor-based powertrain for high-performance electric vehicle," *IEEE Transactions on Transportation Electrification*, vol. 6, no. 3, pp. 1199–1210, 2020.
24. N. Farrokhzad Ershad, R. Tafazzoli Mehrjardi, and M. Ehsani, "Efficient flywheel-based all-wheel-drive electric powertrain," *IEEE Transactions on Industrial Electronics*, vol. 68, no. 7, pp. 5661–5671, 2021.
25. X. Sun, M. Cheng, W. Hua, and L. Xu, "Optimal design of double-layer permanent magnet dual mechanical port machine for wind power application," *IEEE Transactions on Magnetics*, vol. 45, no. 10, pp. 4613–4616, Oct. 2009.
26. X. Sun and M. Cheng, "Thermal analysis and cooling system design of dual mechanical port machine for wind power application," *IEEE Transactions on Industrial Electronics*, vol. 60, no. 5, pp. 1724–1733, May 2013.
27. T. A. LIPO, "The d-q Equations of a Synchronous Machine," in *Analysis of Synchronous Machines*, 2nd ed, Boca Raton, FL: CRC Press, 2012, pp. 168–169.
28. J. Liu, Y. Gao, S. Geng, and L. Wu, "Nonlinear control of variable speed wind turbines via fuzzy techniques," *IEEE Access*, vol. 5, pp. 27–34, 2017.
29. "Metal Strength Chart: A detailed guide to metal strengths - eziil - best metal fabrication software," *Eziil*, <https://eziil.com/steel-strengths/>.
30. G. O. Kremer et al., "Application of axiomatic design, TRIZ, and mixed integer programming to develop innovative designs: A Locomotive Ballast Arrangement Case Study," *The International Journal of Advanced Manufacturing Technology*, vol. 61, no. 5–8, pp. 827–842, Jan. 2012.
31. R. M. Prasad and M. A. Mulla, "A novel position-sensorless algorithm for field-oriented control of DFIG with reduced current sensors," *IEEE Transactions on Sustainable Energy*, vol. 10, no. 3, pp. 1098–1108, Jul. 2019.

Disclaimer/Publisher's Note: The statements, opinions and data contained in all publications are solely those of the individual author(s) and contributor(s) and not of MDPI and/or the editor(s). MDPI and/or the editor(s) disclaim responsibility for any injury to people or property resulting from any ideas, methods, instructions or products referred to in the content.